Infrared optical properties of amorphous and nanocrystalline Ta_2O_5 thin films

T. J. Bright,[1] J. I. Watjen,[1] Z. M. Zhang,[1,a)] C. Muratore,[2,3] A. A. Voevodin,[2] D. I. Koukis,[4] D. B. Tanner,[4] and D. J. Arenas[5]
[1]*George W. Woodruff School of Mechanical Engineering, Georgia Institute of Technology, Atlanta, Georgia 30332, USA*
[2]*Nanoelectronic Materials Branch, Materials and Manufacturing Directorate, Air Force Research Laboratory, Wright Patterson AFB, Ohio 45433, USA*
[3]*Department of Chemical and Materials Engineering, University of Dayton, Dayton, Ohio 45469, USA*
[4]*Department of Physics, University of Florida, Gainesville, Florida 32611, USA*
[5]*Department of Physics, University of North Florida, Jacksonville, Florida 32254, USA*

(Received 12 December 2012; accepted 11 August 2013; published online 28 August 2013)

The optical constants of tantalum pentoxide (Ta_2O_5) are determined in a broad spectral region from the visible to the far infrared. Ta_2O_5 films of various thicknesses from approximately 170 to 1600 nm are deposited using reactive magnetron sputtering on Si substrates. X-ray diffraction shows that the as-deposited films are amorphous, and annealing in air at 800 °C results in the formation of nanocrystalline Ta_2O_5. Ellipsometry is used to obtain the dispersion in the visible and near-infrared. Two Fourier-transform infrared spectrometers are used to measure the transmittance and reflectance at wavelengths from 1 to 1000 μm. The surface topography and microstructure of the samples are examined using atomic force microscopy, confocal microscopy, and scanning electron microscopy. Classical Lorentz oscillators are employed to model the absorption bands due to phonons and impurities. A simple model is introduced to account for light scattering in the annealed films, which contain micro-cracks. For the unannealed samples, an effective-medium approximation is used to take into account the adsorbed moisture in the film and a Drude free-electron term is also added to model the broad background absorption. © *2013 AIP Publishing LLC*. [http://dx.doi.org/10.1063/1.4819325]

I. INTRODUCTION

Tantalum pentoxide (Ta_2O_5) is a high refractive index dielectric with chemical stability at high temperatures and a melting point of 1785 °C, and is thus suitable for high-temperature applications. Ta_2O_5 films have been used or have potential applications in thin-film capacitors,[1] microelectronics,[2] anti-reflection coatings,[3] multilayer optical coatings,[4,5] corrosion resistant protective coatings,[5] and infrared (IR) emissivity modulating devices.[6] Knowledge of the optical properties of Ta_2O_5 is needed for the design of devices that tailor radiative properties such as anti-reflection and multilayer coatings.

Ta_2O_5 films can be deposited by various methods of physical vapor deposition (PVD) or chemical vapor deposition (CVD).[2] Different deposition methods may result in films that have an amorphous phase (a-Ta_2O_5) or two distinct crystal phases depending on the annealing, that is, an orthorhombic β-Ta_2O_5 and a hexagonal δ-Ta_2O_5.[2,7] In addition, there is also a high-temperature tetragonal α-Ta_2O_5 phase that forms at temperatures of approximately 1360 °C.[8] Phase transformation at much lower temperatures can also occur in nanostructured Ta_2O_5.[9] The majority of literature on the optical constants has concentrated on the ultraviolet (UV), visible, and near-IR properties.[4,10–14] The optical constants for a variety of dielectric films, deposited using electron-beam evaporation, have been determined and tabulated from 0.6 to 12 μm in Ref. 15. It was shown that Ta_2O_5 has a refractive index around 2.0 with negligible absorption from 0.6 up to 10 μm.[15] Chandrasekharan *et al.*[16] reported the mid-IR properties of Ta_2O_5 films and studied the development of a SiO_2 layer at the interface between the film and the Si substrate due to heat treatment. Franke *et al.*[17,18] investigated the optical properties of amorphous and crystalline Ta_2O_5 films from the deep-UV to far-IR using spectroscopic ellipsometry. The dielectric function was modeled based on the line-shape analysis up to a wavelength of 40 μm. However, strong phonon modes exist in Ta_2O_5 at wavenumbers between 200 and 300 cm^{-1} (or wavelengths from 50 to 33 μm).[19] In order to fully describe the far-IR dielectric function of Ta_2O_5 films, it is imperative to consider these phonon modes in the dielectric function model. The study of the far-IR properties of materials may be useful in designing absorption-based filters as well as in understanding the atomic bonding structures.[19]

In this work, the dielectric functions of amorphous and nanocrystalline Ta_2O_5 films are determined, at wavenumbers from 10 to 20 000 cm^{-1}, by analyzing ellipsometric measurements in the visible and near-IR regions and by fitting the transmittance and reflectance measured with Fourier-transform IR (FTIR) spectrometers from the near- to far-IR regions. Thin Ta_2O_5 films are deposited on Si substrates using reactive magnetron sputtering. The phase and structure of the as-deposited and annealed samples are also characterized. The location and strength of individual phonon bands

a)Electronic mail: zhuomin.zhang@me.gatech.edu

are determined in the mid- and far-infrared regions. The effect of cracking in the annealed films is considered using a volume-scattering model. The effects of free carriers and adsorbed water moisture in the amorphous films are also considered in the development of the dielectric function model.

II. SAMPLE FABRICATION AND CHARACTERIZATION

A magnetron sputtering system, described previously,[20] was used to deposit thin Ta_2O_5 films on Si substrates. The films were reactively sputtered from a Ta target of 99.9% purity in an Ar/O_2 environment to facilitate the reactive formation of the oxide. During the deposition process, the power was maintained at 30 W and the substrate temperature was held at 100 °C. The flow rates of Ar and O_2 gases with 99.999% purity were 22 sccm and 2.5 sccm, respectively. The substrate thickness and properties are different for some of the samples. Detailed parameters of the six samples used for the present study are listed in Table I. Two of them were left as-deposited and the rest were annealed in air at 800 °C for 1 h. The deposition parameters such as gas flow rates and substrate temperature were chosen according to the literature[21–26] in order to obtain high-quality Ta_2O_5 films.

X-ray diffraction (XRD) measurements of the annealed and as-deposited samples were performed using a Rigaku D-Max diffractometer in a Bragg-Brentano configuration. A test film was annealed at various temperatures in air. Annealing in air at 800 °C for 1 h yielded well-defined XRD patterns; therefore, all the annealed samples were treated under the same annealing condition. Figure 1 shows the XRD profile for TaO-3a that matches well with the orthorhombic β-phase (JCPDS: 25-0922), although some closely spaced peaks appear to be merged due to broadening.[7,27,28] The prominent peak in the (001) plane suggests an anisotropic crystalline orientation due to the stress effect. Similar results were obtained for other annealed samples, but are not shown. It should be noted that there exists a hexagonal δ-phase of Ta_2O_5 (JCPDS: 19-1299) that has a diffraction pattern nearly overlapping that of the β-phase Ta_2O_5.[7,8] Both of these crystal phases are reported to occur in the literature at annealing temperatures close to that used in the present study.[2,7,8,27,28] Hence, it is possible that both phases exist in the annealed films. The identification of the β-phase is confirmed by the broadness of the peaks and the existence of several minor peaks in the XRD pattern. Therefore, it is presumed that the annealed samples are primarily orthorhombic β-phase. The XRD peak associated with (001) plane in Fig. 1 is used to estimate the crystalline size, which is about 40 nm, according to Scherrer's formula.[29] Hence the annealed films are identified as containing nanocrystalline Ta_2O_5. Note that the peaks at $2\theta = 29°$ and 37° are broadened due to the merging of multiple diffraction orders. The unannealed or as-deposited samples are amorphous as there are no distinct peaks in the XRD profiles, which are not shown here. To verify the composition of the fabricated films, X-ray photoelectron spectroscopy (XPS) was performed for an annealed and an unannealed sample after all the spectroscopic measurements. The samples were heated to 200 °C in ultrahigh vacuum to remove surface water. The analysis of the XPS data for the Ta 4f peak position and the area ratio of Ta 4f and O 1s peaks reveals close to stoichiometric Ta_2O_5 in both the annealed and unannealed samples.

The surface topography of the samples was measured using a Veeco Dimension 3100 Atomic Force Microscope (AFM) in tapping mode over an area of either $4 \times 4\ \mu m^2$ or $3 \times 3\ \mu m^2$. The AFM probe is an uncoated *n*-type Si probe whose tip radius is 10 nm. The measured roughness for each

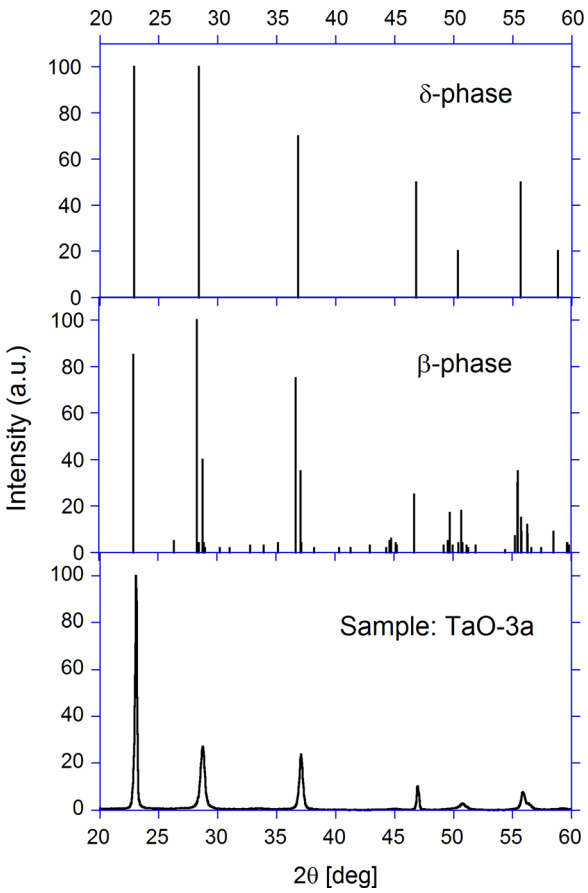

FIG. 1. X-ray diffraction profile of an annealed Ta_2O_5, sample TaO-3a, also shown are the powder diffraction files for δ-Ta_2O_5 and β-Ta_2O_5. Other annealed samples show nearly identical XRD profiles. Note that the as-deposited samples do not show any peaks in their XRD profiles, which are therefore not shown here.

TABLE I. Sample identification (ID) and parameters. In the sample ID, the last letter "u" indicates that it was unannealed (or as-deposited) and "a" indicates that it was annealed at 800 °C in air for 1 h. The unannealed Ta_2O_5 samples TaO-1u and TaO-2u are amorphous. The annealed four samples are nanocrystalline Ta_2O_5. The RMS roughness of the film is obtained from AFM.

Sample ID	Substrate thickness (μm)	RMS roughness (nm)	Film thickness (Ellipsometry) (nm)	Film thickness (FTIR) (nm)
TaO-1u	432	4.1	1588	1589
TaO-2u	432	2.6	492	506
TaO-3a	432	14.5	1017	1035
TaO-4a	432	20.4	462	478
TaO-5a	750	3.6	347	353
TaO-6a	750	3.3	174	179

sample is listed in Table I. The AFM topography of two samples is shown in Fig. 2. The unannealed sample TaO-2u, shown in Fig. 2(a), does not contain any cracks. The presence of cracks can clearly be seen in Fig. 2(b) for the annealed sample TaO-3a. As can be seen from the AFM images and Table I, the cracks have increased the root-mean-square (RMS) roughness that significantly exceeds the actual local surface roughness. Similar cracks in annealed Ta_2O_5 films have been reported by other researchers. The crack development is mainly due to the considerable mismatch between the thermal expansion coefficients of Ta_2O_5 (4.68×10^{-6} K^{-1}) and the Si substrate (1.10×10^{-6} K^{-1}). The mismatch was reported in the literature as the main contributor to both stress and refractive index variation for the Ta_2O_5 films.[30] The compressive stress develops as the sample is heated to the annealing temperature, while the tensile stress develops during the sample cooling. For the two thinnest films, samples TaO-5a and TaO-6a, the stress may not be significant enough and hence the RMS roughness is on the same order as that of the amorphous films.

In addition, images of the surfaces were taken with an Olympus LEXT 3D Material Confocal Microscope over a larger surface area of 43×43 μm^2. Two microscope images are displayed in Fig. 3. Figure 3(a) shows the unannealed sample, TaO-2u, which has a much smoother surface and no cracking. Figure 3(b) shows the surface of an annealed sample TaO-3a. The scaly appearance is due to cracking that occurs during annealing. Cross-sectional images of two films were also taken using scanning electron microscopy (SEM) at an inclined angle of approximately 45° to study their microstructure, as shown in Fig. 4. The unannealed sample TaO-1u, shown in Fig. 4(a), does not display significant cracking or roughness. It can be seen in Fig. 4(b) that the annealed sample TaO-4a contains cracks that penetrate through the film. These cracks contribute to volumetric scattering and optical losses in the sample and need to be included in the modeling of the radiative properties that will be discussed in Sec. III C.

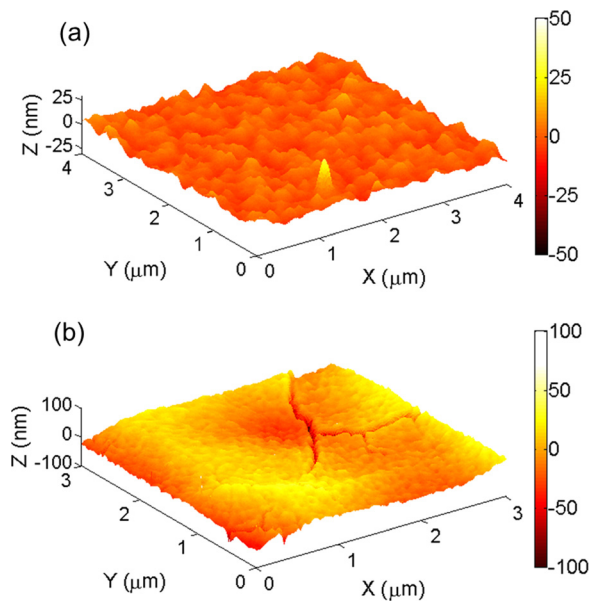

FIG. 2. AFM topographies of (a) sample TaO-2u and (b) sample TaO-3a.

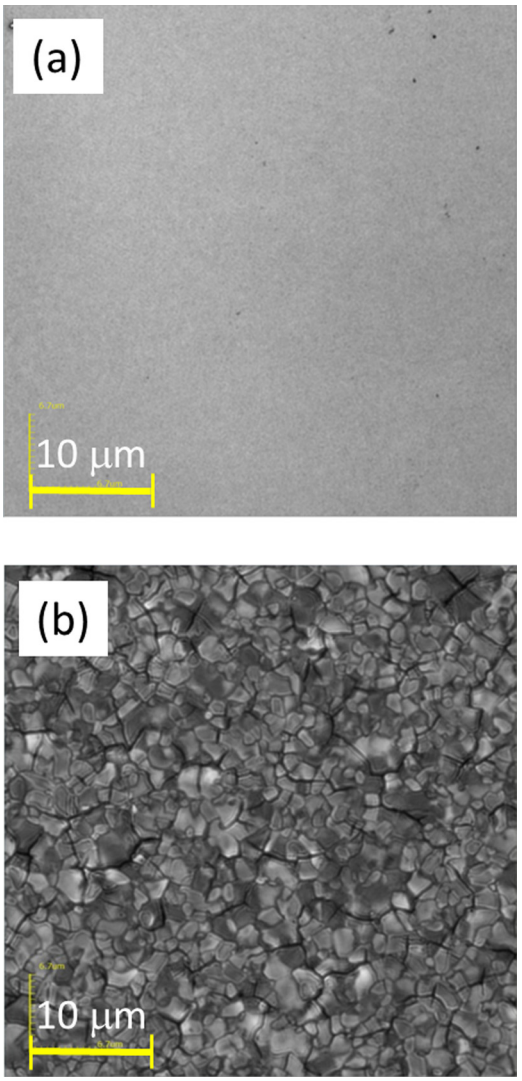

FIG. 3. Confocal microscope images of (a) sample TaO-2u and (b) sample TaO-3a.

III. SPECTROSCOPIC MEASUREMENTS AND ANALYSIS

A. Instrumentation

A J.A. Woollam M-2000 ellipsometer was used to perform variable angle, room temperature ellipsometry measurements of the Ta_2O_5 samples in the wavelength range from 500 to 1000 nm with a resolution of 1.6 nm. Data for three incidence angles (65°, 70°, and 75°) were collected and used to extract the thickness and dispersion of each film in the visible and near-IR regions. The built-in algorithm in the CompleteEase software was used to optimize the regression parameters as well as to estimate the standard error in the ellipsometry parameters of the fitting.

An ABB Bomem FTLA-2000 FTIR was used to measure the normal transmittance of the Ta_2O_5 samples as well as the near normal reflectance of the samples for incidence on either the substrate or the film side at room temperature. Measurements were taken in the wavenumber range from approximately 500 to 10 000 cm^{-1} at 4 cm^{-1} resolution. The spectrometer was purged with nitrogen gas to minimize CO_2

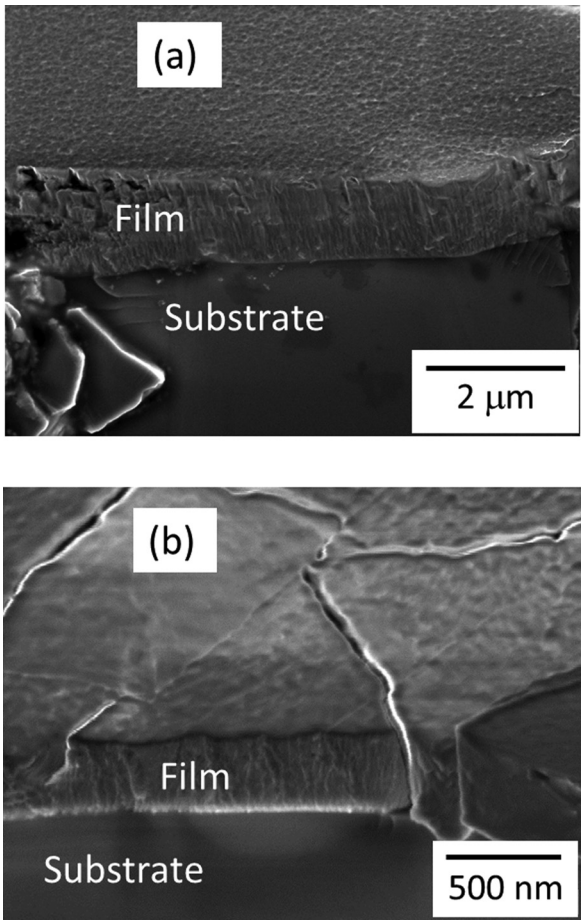

FIG. 4. SEM cross section images of (a) sample TaO-1u and (b) sample TaO-4a.

and water vapor absorption in the ambient air. Reflectance measurements rely on comparisons with that of an Au mirror as the reference, whose reflectance was calculated based on the optical constants of Au taken from Ref. 31 and used to deduce the sample reflectance. Additional details about the measurement procedure and uncertainties can be found from the previous publications and will not be repeated here.[20,32]

A Bruker 113v FTIR spectrometer was used to measure the transmittance and film-side reflectance in the spectral region from 10 to 600 cm^{-1} at a resolution of 2 cm^{-1}. The transmittance was measured relative to a Si wafer to reduce the interference effect in the substrate. A correction procedure as discussed later is used to obtain the transmittance of the film-substrate composite. The reflectance was measured relative to an Al mirror, and the measurement results were corrected to account for the reflectance of Al. The mirror was frequently replaced with fresh-deposited Al film to avoid oxidation that may change the surface reflectance.

The transmittance data agree well in the overlapping region between the purged FTIR and the vacuum far-IR spectrometer results. The reflectance measurement by the far-IR spectrometer is more reliable and allows the identification of some offset in the mid-IR measurements in some samples. Most of the analysis discussed in Sec. III B is based on the transmittance data, and the measured reflectance spectra are used to check the reasonableness of the model predictions. The thickness and high-frequency optical constants of the film were fitted using the near- and mid-IR measurements from the ellipsometer and FTIR, while the phonon modes were fitted with the far-IR data from about 20 to 1000 cm^{-1} using the classical Lorentz oscillator model discussed in Sec. III B.

B. Dielectric function model

The optical constants of the Ta_2O_5 films are determined by the line-shape analysis using the description of the dielectric function given as[33]

$$\varepsilon(\omega) = \varepsilon' + i\varepsilon'' = \varepsilon_\infty - \frac{\omega_{p,0}^2}{\omega^2 + i\gamma_0\omega} + \sum_{j=1}^{N} \frac{\omega_{p,j}^2}{\omega_j^2 - \omega^2 - i\gamma\omega}. \quad (1)$$

Usually, the first term on the right hand side of Eq. (1) is taken as a constant to reflect high-frequency contributions. In the present study, ε_∞ is calculated from the refractive index following the Cauchy dispersion

$$n(\lambda) = \sqrt{\varepsilon_\infty} = A + \frac{B}{\lambda^2}, \quad (2)$$

where λ is the wavelength in vacuum and constants A and B can be obtained from ellipsometry data.[20] Note that band gap absorption is not considered since the band gap of Ta_2O_5 is greater than 4 eV.[10,18] This treatment allows Eq. (1) to represent the dielectric function from $\lambda = 500$ nm all the way to the far-IR. The second term is a Drude free-electron term, which is included only for the unannealed samples due to the residual broadband absorption. The Drude term contains two adjustable parameters, namely, the plasma frequency $\omega_{p,0}$ and scattering rate γ_0. The third term in Eq. (1) is the sum of N Lorentz oscillators, which correspond to the phonon absorption bands in the far-IR region. Each individual oscillator j has a center frequency ω_j, a plasma frequency $\omega_{p,j}$, and a damping coefficient γ_j. Due to the practical limitations caused by the uncertainty in the data, the oscillators in the model may not correspond to all of the infrared-active phonon modes present in the material, especially if modes are very close in frequency or very weak. Stronger and broader phonon bands may mask some weaker phonon modes. The phonon modes can be predicted by *ab initio* simulation according to the crystalline structure for similar materials;[34] however, not all of the modes may manifest in experimental measurements.[19] In addition, defect modes may arise from impurities present in the films.[17,18] Note that impurity modes are not distinguished from the actual phonon modes of Ta_2O_5 in the experimentally determined dielectric function. Thus, the oscillators obtained by fitting the IR spectra should be considered as effective phonon modes and represent the overall lattice vibration contributions. The dielectric function model does however provide an accurate description of the optical properties of the material in a broad spectral region and captures the behavior of major phonon resonances well.

The unannealed samples also have an absorption band around the wavenumber of 3400 cm^{-1}, which is characteristic of moisture absorption.[17] In order to account for the

existence of moisture in the unannealed samples, the Bruggeman effective medium approximation (EMA) is used to determine the effective dielectric function of the film, ε_{eff}, assuming that a small amount of water is randomly dispersed in the Ta_2O_5 film[17,35]

$$(1-f)\frac{\varepsilon-\varepsilon_{\text{eff}}}{\varepsilon+2\varepsilon_{\text{eff}}}+f\frac{\varepsilon_{\text{w}}-\varepsilon_{\text{eff}}}{\varepsilon_{\text{w}}+2\varepsilon_{\text{eff}}}=0, \tag{3}$$

where f is the volume fraction of water, ε is calculated from Eq. (1), and ε_{w} is the dielectric function of water taken from Downing and Williams.[36] Note that the EMA prediction of ε_{eff} is taken as the dielectric function of the moist Ta_2O_5 film and is used to calculate the radiative properties of the film-substrate composite. The additional parameter f is only sensitive in the water absorption region and can be determined by fitting the transmittance in the near- to mid-IR region.

C. Fitting procedure

In the region for ellipsometry measurements, the Si substrate is opaque and thin-film optics can be used to fit the ellipsometry parameters Ψ and Δ according to the ratio of the Fresnel reflection coefficients for p-polarized (r_{p}) and s-polarized (r_{s}) waves as follows:[17,20]

$$R=\frac{r_{\text{p}}}{r_{\text{s}}}=\tan(\Psi)\exp(i\Delta). \tag{4}$$

Note that the quantity Ψ is related to the relative intensity of the reflected lights of the two polarizations and Δ is the relative difference of their phases. Both quantities can be calculated with thin-film optics by assuming a homogeneous thin film with smooth parallel interfaces on an opaque substrate. Multiple incidence angles are used to ensure a reliable determination of parameters A and B in Eq. (2) and the film thickness.

The transmittance and reflectance spectra obtained by the FTIR spectrometers were fit using the optical model for a coherent film on a thick incoherent substrate.[33,37] This is a reasonable assumption considering the relatively low spectral resolution of $4\,\text{cm}^{-1}$ in the near-and mid-IR region. The transmittance and reflectance for a thin film on a thick substrate can be expressed as follows:[38]

$$T=\frac{\tau_{\text{a}}\tau_{\text{s}}\tau_{\text{i}}}{1-\rho_{\text{s}}\rho_{\text{b}}\tau_{\text{i}}^2}, \tag{5}$$

$$R_{\text{f}}=\rho_{\text{a}}+\frac{\rho_{\text{s}}\tau_{\text{a}}^2\tau_{\text{i}}^2}{1-\rho_{\text{s}}\rho_{\text{b}}\tau_{\text{i}}^2}, \tag{6}$$

$$R_{\text{s}}=\rho_{\text{s}}+\frac{\rho_{\text{b}}\tau_{\text{s}}^2\tau_{\text{i}}^2}{1-\rho_{\text{s}}\rho_{\text{b}}\tau_{\text{i}}^2}, \tag{7}$$

where the subscript f or s in the reflectance R signifies the film-side or substrate-side incidence. In Eqs. (5)–(7), τ_i is the internal transmissivity of the substrate, τ_{a} and ρ_{a} are the transmittance and reflectance at the air-film interface when the substrate is semi-infinite, ρ_{b} is the reflectance for incidence from the substrate at the interface between the substrate-air, assuming that the substrate is nonabsorbing and semi-infinite, and τ_{s} and ρ_{s} are the transmittance and reflectance at the air-substrate interface when both media are semi-infinite.[33,37,38] Most of the fitting is based on the transmittance only and compared with the reflectance data to confirm the fitting results. The reason for using transmittance only is because the reflectance measurements are subject to a larger relative uncertainty of around 5%.

The interference effect in the Si substrate is inevitable in the measured far-IR spectrum. To reduce the interference effect, the transmittance of the sample was measured relative to a bare Si substrate. The optical constants of Si were taken from Ref. 31 and were modified to account for the additional absorption around $900\,\text{cm}^{-1}$ caused by an O-H band as discussed previously. Four of the samples were deposited on $432\pm5\,\mu$m thick Si substrates with a resistivity of 20 Ω cm, and the remaining two were deposited on $750\pm25\,\mu$m thick Si substrates (see Table I) with a resistivity between 10 and 100 Ω cm as specified by the manufacturer. The resistance of the thinner Si substrate was determined by fitting the well-known Drude model for boron-doped Si to the transmittance of the Si in the far-IR spectrum according to Fu and Zhang[39] and references therein. The doping level was thus estimated to be $6.67\times10^{14}\ \text{cm}^{-3}$. The transmittance spectrum of Si calculated from the incoherent formula based on the Drude model was used to deduce the transmittance data of the samples in the far-IR region from the relative measurements. The Drude model is also used to calculate the radiative properties of the film-substrate composite in the far-IR region ($\lambda>20\,\mu$m) in the line-shape analysis. The effect of the Drude term is negligible at wavelengths shorter than $20\,\mu$m. It should be noted that the far-IR measurements were not performed for the last two samples listed in Table I with the thicker Si substrates. It is shown by comparison with the transmittance of a bare Si substrate that the optical constants from Refs. 20 and 31 are suitable for modeling the near- and mid-IR radiative properties with the thicker substrate, whose resistivity does not need to be precisely determined.

For the annealed samples with cracks, the transmittance and the film-side reflectance of the FTIR data exhibit some attenuation towards the near-IR end of the spectra. Attempts were initially made to include a surface roughness term according to the scalar scattering theory.[33,40] The predicted results also showed an attenuation in the substrate-side reflectance that contradicts with the experimental observation. In addition, when the ellipsometry data were analyzed, accounting for roughness did not improve the fitting. Therefore, the cracking effect cannot be well described by surface scattering. A careful examination of Eqs. (5)–(7) reveals that τ_{a} is the only term that appears in T and R_{f} but not R_{s}. A volumetric scattering model is considered in the final analysis to better model the observed trends due to cracking of the thick annealed samples, i.e., TaO-3a and TaO-4a. It is assumed that scattering results in a reduction only in the transmission through the film, and the attenuation is wavelength dependent according to

$$\tau_{\text{a}}'=\tau_{\text{a}}\left(1-\frac{S_{\text{f}}^4}{\lambda^4}\right). \tag{8}$$

Here, S_f is a fitting parameter that is related to the scattering cross-sectional area and the defect density, assuming independent scattering by small particles that follow Rayleigh scattering.[40,41] When τ_a in Eqs. (5) and (6) are substituted by τ'_a from Eq. (8), both the transmittance and reflectance of the film side of the sample are reduced, while the substrate-side reflectance given in Eq. (7) is unaffected. This gives a reasonable interpretation of the experimental results to be discussed in Sec. IV B. It should be noted that volume scattering may also arise due to relatively large grains in the film. Hence, S_f may be considered as an effective lumped sum of the volume scattering contribution.

The predicted radiative properties are fitted to the measured FTIR transmittance spectra using a simplex optimization algorithm that minimizes the standard error of estimate (SEE).[42,43] It is assumed that ε_∞ is the same as the average value obtained for either the unannealed or annealed samples from the ellipsometry data according to Eq. (2). The film thickness is related to the interference fringes and determined by fitting the FTIR data in the near- to mid-IR region. The obtained thickness is then used to fit the parameters in Eqs. (1) and (3) using far-IR transmittance.

IV. RESULTS AND DISCUSSION

A. Ellipsometric results

The optical constants at wavelengths from 500 to 1000 nm are determined from the ellipsometry data. Each sample was fit individually to obtain the parameters A and B in the Cauchy dispersion, Eq. (2), and the film thickness. The absorption is neglected because the interband transitions occur at photon energies greater than 4 eV.[10,17,18] The resulting A and B values change little from sample to sample; therefore, only the averages of all A and B values for the two unannealed samples and those for the annealed samples are reported here. For the unannealed samples, the average A and B are 2.06 and 0.025 μm^2, respectively. For the annealed samples the average values of A and B are 2.10 and 0.024 μm^2, respectively. All of the uncertainties in A and B are less than 0.02 and 0.001 μm^2, respectively. Table I shows the thickness obtained from fitting the ellipsometry data with the Cauchy model. The agreement between the ellipsometry data and the model is very good for the unannealed samples as well as for the thinnest annealed samples. The average mean squared error (MSE) for the two annealed samples TaO-3a and TaO-4a with cracks is about five times larger than the rest. However, the coefficients A and B are all very close. The resulting refractive indices of $n = 2.16$ and 2.20 for unannealed and annealed Ta_2O_5 films, respectively, agree with the typical values reported in the literature at $\lambda = 500$ nm.[4,12–14,17]

B. Comparison of the measured and calculated radiative properties

While ε_∞ in Eq. (1) can be fit using the FTIR data, for consistency, it is taken instead from the Cauchy dispersion from Eq. (2) based on ellipsometry measurements. The film thickness is also fit using near- and mid-IR transmittances, which are sensitive to the film thickness due to the interference effect. Despite the existence of cracking, the film thicknesses obtained from the ellipsometer are quite consistent with those from the FTIR measurements as shown in Table I. The far-IR transmittance is used to fit the phonon oscillator parameters and the results are listed in Table II. For the unannealed samples, the transmittance measured by FTIR is compared to the best fit curves as shown in Fig. 5. The agreement is generally satisfactory throughout the concerned spectral region. The dips in the far-IR transmission shown in Fig. 5(a) are due to interaction of light with phonon vibration modes in Ta_2O_5. Each of these dips is represented by an oscillator in the dielectric model. Some of the dips may also be caused by the Si substrate especially around 610 cm^{-1}, where there is a dip due to Si absorption. Due to the uncertainty of the data, very weak phonon features are difficult to resolve.

The Drude term results in broad absorption and the plasma frequency and scattering rate are found to be $\omega_{p,0} = 6490\ cm^{-1}$ and $\gamma_0 = 6.5 \times 10^5\ cm^{-1}$ from the fitting. This extreme broadness can be attributed to the fact that the samples are amorphous and thus have a very large electron scattering rate. Based on the Drude parameters, the resistivity of the sample can be estimated to be 0.9 Ω cm, which would be typical of a lightly doped material. The existence of free electrons in the unannealed samples is presumably due to a slight oxygen deficiency or sub-stoichiometry during the growth process, although other possibilities also exist.[2,6,16] According to Kulisch *et al.*,[44] suboxides of Ta can contribute to a broadband absorption around 900 cm^{-1}, which is evident from Fig. 4(a). However, the XPS analysis does not show any apparent suboxides of Ta in both the annealed and unannealed samples, suggesting that the oxygen deficiency is insignificant.

The presence of moisture in the film is apparent from the dip in the transmittance around 3400 cm^{-1}. It is found using the EMA analysis from Eq. (3) that a volume fraction of water of 5% works best to model the moisture contribution to the dielectric function. The addition of water matches the dip well at 3400 cm^{-1}, but is not broad enough to match the valley in transmittance. Therefore, another weak oscillator is added around 3000 cm^{-1} to the dielectric function model ($j = 6$ in Table II). This results in satisfactory agreement between the model prediction and the transmittance in the mid-IR region as shown in Fig. 5(b).

TABLE II. Parameters for the Lorentz oscillators. Note that the parameters that determine ε_∞ from the ellipsometric measurements are ($A = 2.06$, $B = 0.025\ \mu m^2$ for amorphous Ta_2O_5; $A = 2.10$, $B = 0.024\ \mu m^2$ for nanocrystalline Ta_2O_5).

	Amorphous			Nanocrystalline		
j	ω_j (cm^{-1})	$\omega_{p,j}$ (cm^{-1})	γ_j (cm^{-1})	ω_j (cm^{-1})	$\omega_{p,j}$ (cm^{-1})	γ_j (cm^{-1})
1	266	1040	188	91	260	74
2	500	573	112	214	844	61
3	609	634	88	324	391	73
4	672	408	43	530	1019	142
5	868	277	113	842	372	114
6	3020	373	652			

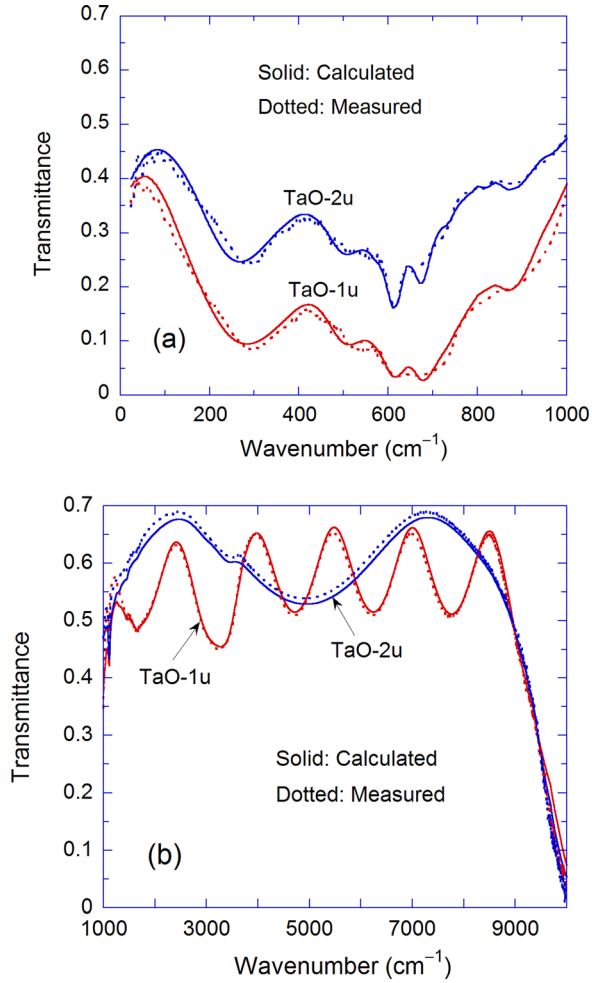

FIG. 5. Transmittance of samples TaO-1u and TaO-2u: (a) far-IR region from 10 to 1000 cm^{-1}; (b) mid-IR region from 1000 to 10 000 cm^{-1}.

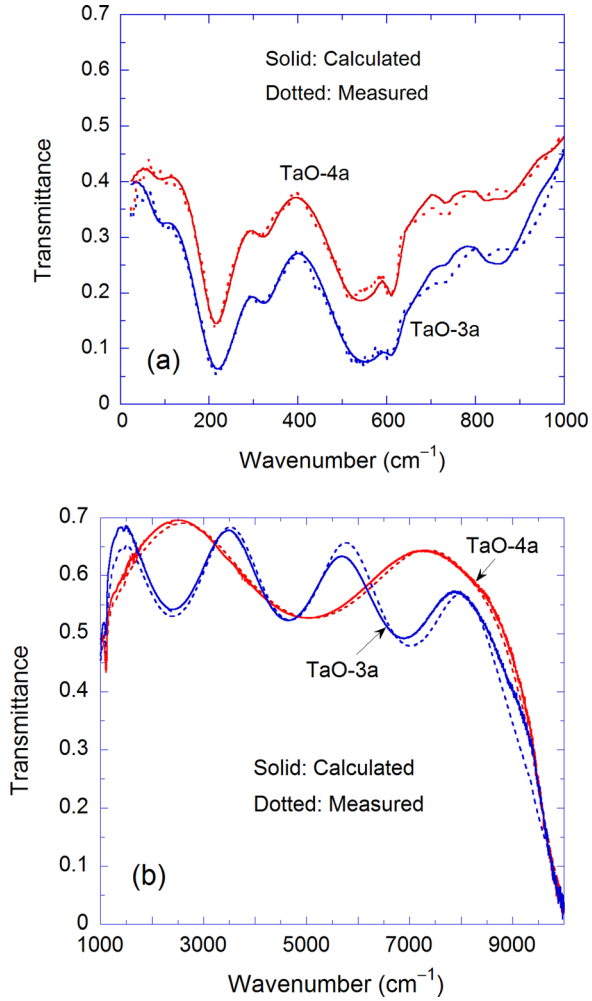

FIG. 6. Transmittance of samples TaO-3a and TaO-4a: (a) far-IR region from 10 to 1000 cm^{-1}; (b) mid-IR region from 1000 to 10 000 cm^{-1}.

The thicker film sample, TaO-1u, exhibits more interference fringes than the thinner film sample, TaO-2u. The free spectral range or wavenumber interval between the interference maxima can be approximated by $1/(2nd)$, where d is the film thickness. Due to absorption around 3000 cm^{-1}, the transmission of the thicker sample drops quite a bit in this region. It should be noted that the minimum transmittance can be estimated from the refractive indices of the film and substrate if absorption is negligible. The introduction of the Drude term is necessary to predict the broadband absorption, allowing the prediction to match the data at the transmittance minima at 4700, 6250, and 7800 cm^{-1}. Note that the drop in transmittance close to 10 000 cm^{-1} is caused by the absorption of the substrate associated with the indirect band gap of Si near 1.1 eV.

The transmittance for two of the annealed samples is shown in Fig. 6. There is no need to include the Drude term in the dielectric function model, since the samples were annealed in air: the reaction with oxygen during the annealing process apparently has improved the stoichiometry. The annealing has removed the absorbed moisture as well. After annealing, the low frequency phonon mode at 266 cm^{-1} shifts to the lower frequencies at 214 cm^{-1} and becomes narrow due to a reduction in the damping coefficient as shown in Table II. This absorption band becomes much narrower and deeper as shown in Fig. 6(a). Another phonon mode is needed to model the small dip around 90 cm^{-1}. From Fig. 6(b), it is evident that there exists a gradual reduction in the transmittance from 3000 to 10 000 cm^{-1} and this reduction is attributed to light scattering due to cracks or grain boundaries inside of the films. The scattering factor S_f for samples TaO-3a and TaO-4a is determined to be 5.3 and 5.1 nm, respectively.

Only the two thicker samples require the addition of volume scattering into the modeling, since cracking was not as significant in the two thinner samples. As shown in Fig. 7, the transmittance calculated for TaO-5a and TaO-6a using the dielectric function model determined for the two thicker annealed samples agrees well with the measured spectra without introducing any volume scattering. The far-IR measurements were not performed on samples TaO-5a and TaO-6a. Strong absorption in the Si substrate near 1100 cm^{-1} can be clearly seen in Fig. 7.

Figure 8 compares the measured and calculated reflectance for TaO-3a for both film-side incidence and substrate-side incidence. There is a gradual attenuation in R_f as shown in Fig. 8(a), but not in R_s as shown in Fig. 8(b). The substrate-side reflectance does not show any decrease toward short wavelengths and this is not typical with surface roughness or

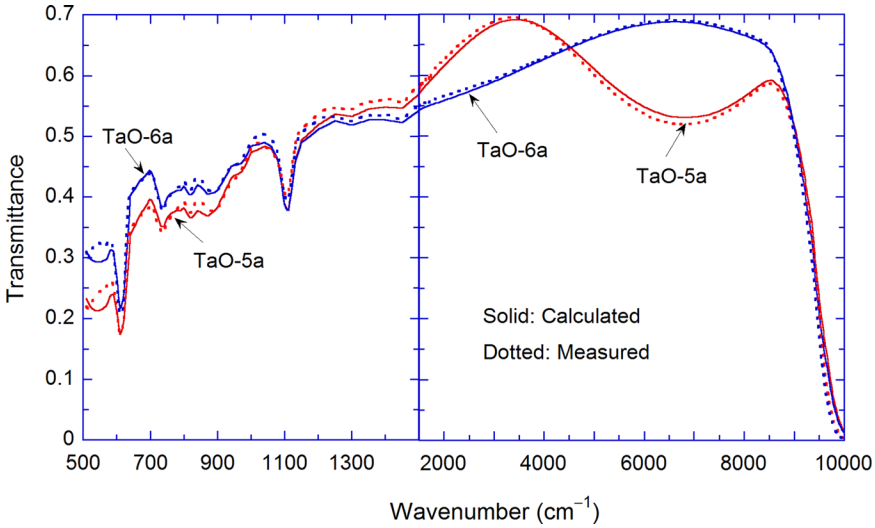

FIG. 7. Transmittance of samples TaO-5a and TaO-6a. Note that the scale is zoomed from 500 to 1500 cm^{-1} to show features in the far-IR region more clearly.

absorption. The volumetric scattering model captures the phenomenon reasonably well, especially considering the simplicity in the model and its assumption of a spherical geometry and Rayleigh-type independent scattering. The model may break down in the short wavelength end of the spectrum, resulting in large disagreement in T and R_f as shown in Figs. 6(b) and 8.

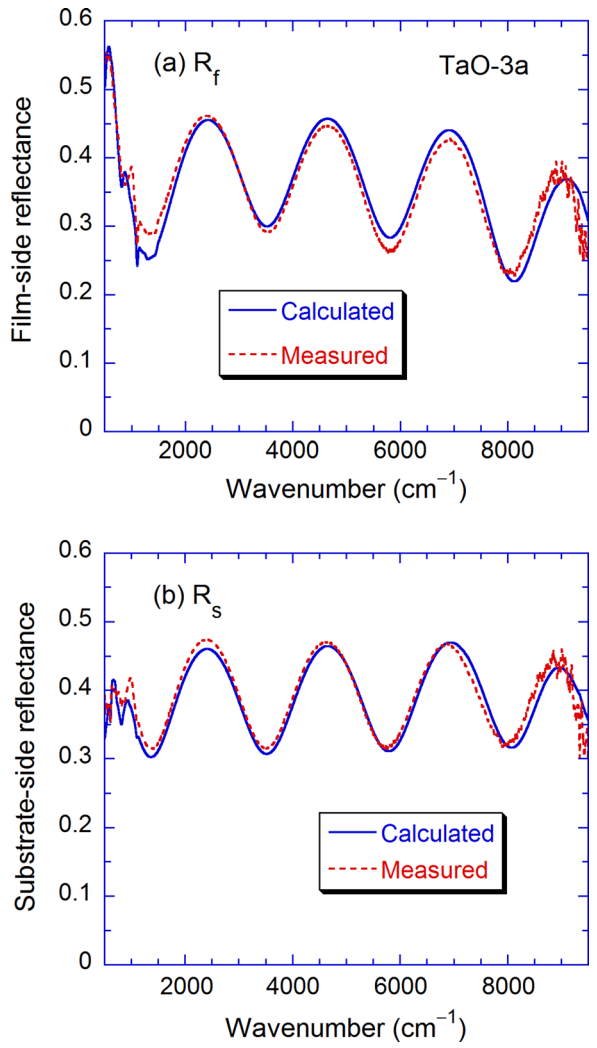

FIG. 8. Reflectance of sample TaO-3a: (a) film-side; (b) substrate-side. Note that the film-side reflectance decreases toward shorter wavelengths due to scattering, while the substrate-side reflectance is unaffected.

It is worth noting that additional reflectance data was also collected but not used in the fitting. Since the reflectance data in the mid-IR region is less reliable than the transmittance data, including them in the fitting would increase the uncertainty. The largest SEE between the model and the experimental data for the transmittance of all the samples was 0.023 and the average was 0.014. The agreement between the reflectance data and the model prediction is good with an average SEE of 0.024.

C. The dielectric functions

The dielectric function obtained for the amorphous Ta_2O_5 films is plotted in Fig. 9 in comparison with that obtained from Franke *et al.*[17] The results are shown from 10 to 1500 cm^{-1} since there is little variation beyond 1500 cm^{-1}, although there are some features due to moisture and the oscillator near 3000 cm^{-1}. Note that the resulting dielectric function is the effective dielectric function expressed in Eq. (3). However, in the spectral region shown in the plots, the effect of 5% water content is negligible, i.e., $\varepsilon_{\text{eff}} \approx \varepsilon$. Toward large wavenumbers, the real part approaches A^2 and the imaginary part becomes very small. The residual ε'' is largely due to the free-electron contribution. The phonon features can be clearly seen from the peaks in the imaginary part.[33,45] The Drude term also increases the imaginary part of the dielectric function toward the smaller wavenumbers. The agreement in the dielectric function obtained from this work and from Ref. 17 is reasonable at wavenumbers exceeding 600 cm^{-1}. However, the phonon modes below 500 cm^{-1} were not resolved in Ref. 17, resulting in a large deviation at smaller wavenumbers.

Figure 10 shows the real and imaginary part of the dielectric function for the annealed samples, compared with those from Ref. 18. A distinction from the amorphous Ta_2O_5 is the sharp peak at the phonon resonance of 214 cm^{-1} in the imaginary part. While the oscillator strength defined as $S_j = \omega_{p,j}^2/\omega_j^2$ is similar to the mode in the amorphous film at 266 cm^{-1}, the reduction in the damping coefficient γ_j gives

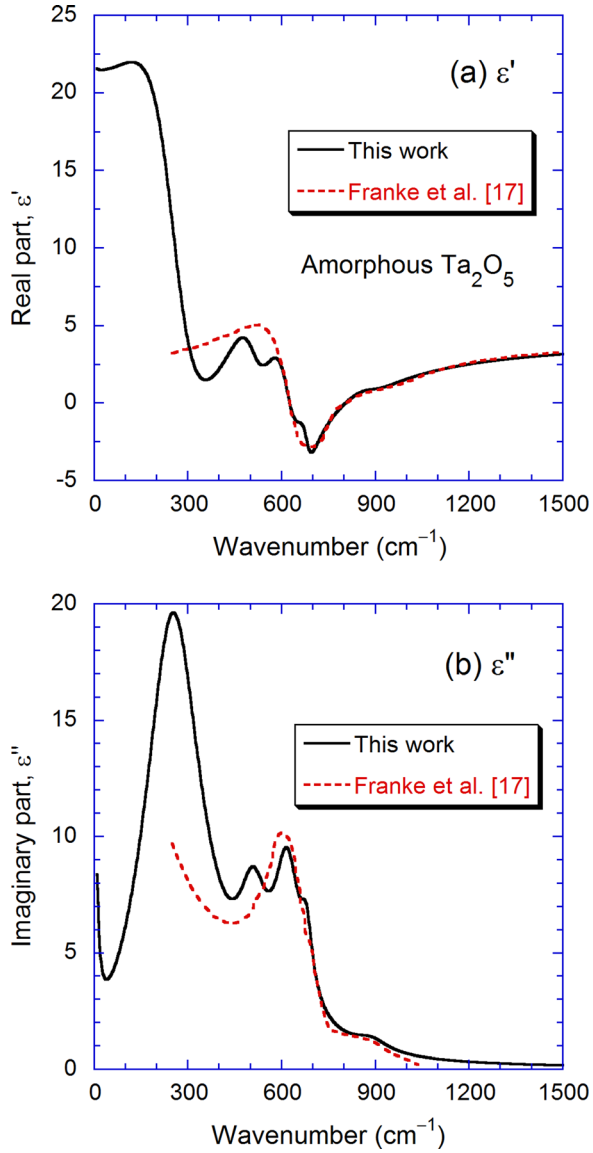

FIG. 9. Fitted dielectric function of the amorphous Ta_2O_5, in comparison with the values from Ref. 17: (a) Real part; (b) Imaginary part.

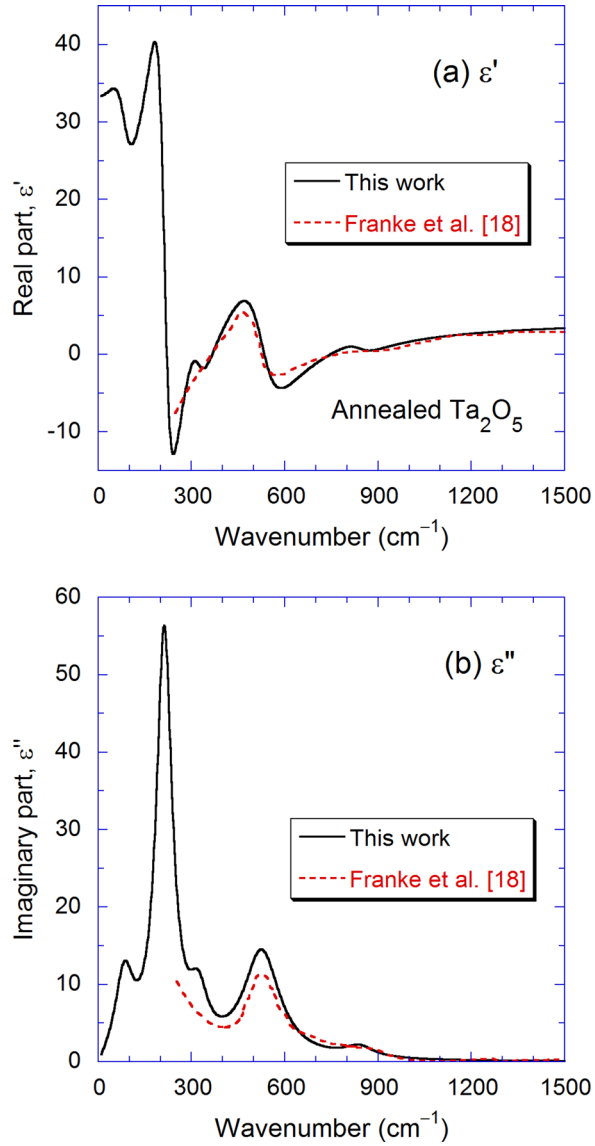

FIG. 10. Fitted dielectric function of the annealed Ta_2O_5, in comparison with the values from Ref. 18: (a) Real part; (b) Imaginary part.

rise to a narrow band in ε''.[45] This results in the stronger absorption observed in the transmittance spectrum shown in Fig. 6(a). Without the Drude term, the imaginary part is negligible at wavenumbers exceeding 1000 cm^{-1}. Hence, the nanocrystalline Ta_2O_5 has negligible absorption in the visible to about 10 μm wavelengths. Towards small wavenumbers, the imaginary part of the dielectric function drops quickly without free-electron absorption, as shown in Fig. 10(b). The real part approaches a dielectric constant of 33 for the annealed films and 23 for the amorphous films. These values are within the range reported for the low-frequency (1 MHz) dielectric constants.[2,27]

V. CONCLUSIONS

The dielectric functions are obtained for amorphous and nanocrystalline thin film samples of Ta_2O_5 deposited by magnetron sputtering. These sputtered films are smooth and of good structural quality and uniform thickness. Samples are amorphous as deposited at the substrate temperature used during deposition. Upon annealing at 800 °C, the samples become nanocrystalline with an orthorhombic phase being dominant. This induces a drastic change in the far-IR optical properties of the film. The low-frequency phonon modes become much sharper in the nanocrystalline samples. The frequencies of the effective phonon modes are determined by a line-shape analysis to quantitatively show the optical phonons in sputtered Ta_2O_5 films. Thermal stresses in the thicker samples after annealing were significant enough to cause cracking and the effect contributes to volume scattering in the sample thus affecting the near-IR transmittance. A simple model is introduced to account for the volumetric scattering in the thin film samples.

ACKNOWLEDGMENTS

This work was mainly sponsored by the Air Force Research Laboratory Thermal Metamaterials Program. Additional support was provided to Z. M. Zhang's group

(for the modeling effort) from the Department of Energy under Contract No. DE-FG02-06ER46343. We would also like to thank Michael Jespersen of UDRI/AFRL for help with the XPS analysis.

[1]S.-D. Cho and K.-W. Paik, Mater. Sci. Eng., B **67**, 108 (1999).
[2]C. Chaneliere, J. L. Autran, R. A. B. Devine, and B. Balland, Mater. Sci. Eng. R **22**, 269–322 (1998).
[3]F. Rubio, J. Denis, J. M. Albella, and J. M. Martinez-Duart, Thin Solid Films **90**, 405 (1982).
[4]A. J. Waldorf, J. A. Dobrowolski, B. T. Sullivan, and L. M. Plante, Appl. Opt. **32**, 5583(1993).
[5]K. Toki, K. Kusakabe, T. Odani, S. Kobuna, and Y. Shimizu, Thin Solid Films **281–282**, 401 (1996).
[6]E. B. Franke, C. L. Trimble, M. Schubert, J. A. Woollam, and J. S. Hale, Appl. Phys. Lett. **77**, 930 (2000).
[7]J. González, M. C. Ruiz, J. B. Rivarola, and D. Pasquevich, J. Mater. Sci. **33**, 4173 (1998).
[8]C. Chaneliere, S. Four, J. L. Autran, and R. A. B. Devine, Microelectron. Reliab. **39**, 261 (1999).
[9]R. S. Devan, W.-D. Ho, S. Y. Wu, and Y.-R. Ma, J. Appl. Cryst. **43**, 498 (2010).
[10]E. E. Khawaja and S. G. Tomlin, Thin Solid Films **30**, 361 (1975).
[11]F. Rubio, J. M. Albella, J. Denis, and J. M. Martinez-Duart, J. Vac. Sci. Technol. **21**, 1043 (1982).
[12]G. A. Al-Jumaily and S. M. Edlou, Thin Solid Films **209**, 223 (1992).
[13]E. Atanassova, G. Aygun, R. Turan, and T. Babeva, J. Vac. Sci. Technol. A **24**, 206 (2006).
[14]J. Zhou, D. Luo, Y. Li, and Z. Liu, Int. J. Mod. Phys. B **23**, 5275 (2009).
[15]J. D. Traylor Kruschwitz and W. T. Pawlewicz, Appl. Opt. **36**, 2157 (1997).
[16]R. Chandrasekharan, S. Prakash, M. A. Shannon, and R. I. Masel, J. Heat Transfer **129**, 27 (2007).
[17]E. Franke, C. L. Trimble, M. J. DeVries, J. A. Woollam, M. Schubert, and F. Frost, J. Appl. Phys. **88**, 5166 (2000).
[18]E. Franke, M. Schubert, C. L. Trimble, M. J. DeVries, and J. A. Woollam, Thin Solid Films **388**, 283 (2001).
[19]H. Ono, Y. Hosokawa, and K. Shinoda, Thin Solid Films **381**, 57 (2001).
[20]T. J. Bright, J. I. Watjen, Z. M. Zhang, C. Muratore, and A. A. Voevodin, Thin Solid Films **520**, 6793 (2012).
[21]O. D. Vol'pyan and P. P. Yakovlev, J. Opt. Technol. **69**, 319 (2002).
[22]E. Atanassova, T. Dimitrova, and J. Koprinarova, Appl. Surf. Sci. **84**, 193 (1995).
[23]S. V. Jagadeesh Chandra, S. Uthanna, and G. Mohan Rao, Appl. Surf. Sci. **254**, 1953 (2008).
[24]K. Chen, M. Nielsen, G. R. Yang, E. J. Rymaszewski, and T.-M. Lu, J. Electron. Mater. **26**, 397 (1997).
[25]C. Guoping, L. Lingzhen, Z. Suixin, and Z. Haokang, Vacuum **41**, 1204 (1990).
[26]J. M. Ngaruiya, S. Venkataraj, R. Drese, O. Kappertz, T. P. Leervad Pedersen, and M. Wuttig, Phys. Status Solidi A **198**, 99 (2003).
[27]P. C. Joshi and M. W. Cole, J. Appl. Phys. **86**, 871 (1999).
[28]T. Dimitrova, K. Arshak, and E. Atanassova, Thin Solid Films **381**, 31 (2001).
[29]A. L. Patterson, Phys. Rev. **56**, 978 (1939).
[30]S. G. Yoon, Y. T. Kim, H. K. Kim, M. J. Kim, H. M. Lee, and D. H. Yoon, Mater. Sci. Eng., B **118**, 234 (2005).
[31]E. D. Palik, *Handbook of Optical Constants of Solids* (Academic Press, San Diego, 1998).
[32]S. Basu, B. J. Lee, and Z. M. Zhang, J. Heat Transfer **132**, 023301 (2010).
[33]Z. M. Zhang, *Nano/Microscale Heat Transfer* (McGraw-Hill Professional, New York, 2007).
[34]P. Clauws, J. Broeckx, and J. Vennik, Phys. Status Solidi B **131**, 459 (1985).
[35]G. L. Carr, S. Perkowitz, and D. B. Tanner, in *Infrared and Millimeter Waves*, edited by W. J. Button (Academic Press, Orlando, 1985), pp. 171–263.
[36]H. D. Downing and D. Williams, J. Geophys. Res. **80**, 1656, doi:10.1029/JC080i012p01656 (1975).
[37]B. J. Lee, Z. M. Zhang, E. A. Early, D. P. DeWitt, and B. K. Tsai, J. Thermophys. Heat Transfer **19**, 558 (2005).
[38]Z. M. Zhang, C. J. Fu, and Q. Z. Zhu, Adv. Heat Transfer **37**, 179 (2003).
[39]C. J. Fu and Z. M. Zhang, Int. J. Heat Mass Transfer **49**, 1703 (2006).
[40]B. J. Lee, V. P. Khuu, and Z. M. Zhang, J. Thermophys. Heat Transfer **19**, 360 (2005).
[41]J. R. Howell, R. Siegel, and M. P. Menguc, *Thermal Radiation Heat Transfer*, 5th ed. (CRC Press, 2010).
[42]Q. Z. Zhu and Z. M. Zhang, in *Nanoparticle Heat Transfer and Fluid Flow*, edited by W. J. Minkowycz, E. M. Sparrow, and J. Abraham (CRC Press/Taylor&Francis Group, 2012), pp. 143–174.
[43]W. H. Press, *Numerical Recipes: The Art of Scientific Computing* (Cambridge University Press, 2007).
[44]W. Kulisch, D. Gilliland, G. Ceccone, L. Sirghi, H. Rauscher, P. N. Gibson, M. Zün, F. Bretagnol, and F. Rossi, J. Vac. Sci. Technol. B **27**, 1180 (2009).
[45]Z. M. Zhang, B. I. Choi, M. I. Flik, and A. C. Anderson, J. Opt. Soc. Am. B **11**, 2252 (1994).